Research Square

Preprints are preliminary reports that have not undergone peer review.
They should not be considered conclusive, used to inform clinical practice,
or referenced by the media as validated information.

First-in-Macaque SPECT Imaging of 131 I-Labeled Extracellular Vesicles Derived from Antler Blastemal Progenitor Cells

Jiajun Ye
Xijing Hospital
Kangxia Yu
Xijing Hospital
Chen Zhou
Xijing Hospital
Yiming Hao
Xijing Hospital
Guoquan Li
Xijing Hospital
Xiaoyan Liang
Xijing Hospital
Guiyu Li
Xijing Hospital
Zifan Zhu
Xijing Hospital
Cai Xu
Xijing Hospital
Pengan Xiang
Xijing Hospital
Jinghui Huang
Xijing Hospital
Jing Wang
Xijing Hospital
Fei Kang
fmmukangf@fmmu.edu.cn

Xijing Hospital

Research Article

Keywords: Extracellular vesicles, Antler blastemal progenitor cells, First-in-Macaque, Iodine-131

Posted Date: November 24th, 2026

DOI: https://doi.org/10.21203/rs.3.rs-11634835/v1

License: This work is licensed under a Creative Commons Attribution 4.0 International License.
Read Full License

Additional Declarations: No competing interests reported.

Abstract

Background

Extracellular vesicles (EVs) serve as promising biomarkers and therapeutic nanocarriers, but their clinical translation is hindered by unstandardized *in vivo* pharmacokinetic and biosafety profiling. Here, we utilized iodine radionuclide-based nuclear imaging to achieve non-invasive, dynamic tracking of antler blastema progenitor cell (ABPC)-derived EVs. We characterized their cross-species biodistribution and kinetics in mice and macaques, establishing a feasible preclinical framework to accelerate EV therapeutic translation.

Methods

We isolated ABPC-derived EVs and radiolabeled them with ^{131}I using the Iodogen protocol, followed by in vitro validation of radiochemical stability. We conducted mouse biodistribution assays, pharmacokinetic modeling and sequential micro-SPECT/CT imaging, alongside quantitative SPECT/CT scans in macaques at 1, 4 and 8 h post-injection. Pharmacokinetic fitting and human phantom dosimetry calculations were completed, and all datasets underwent statistical analysis to facilitate preclinical translational assessment of ABPC-derived EVs.

Results

EVs^{ABPC} with typical cup-shaped morphology and uniform diameters of 100–160 nm were successfully isolated and efficiently radiolabeled with ^{131}I via the Iodogen oxidation protocol. The resultant ^{131}I-EVs^{ABPC} produced a radiochemical yield of 67.6% and attained radiochemical purity greater than 99% post-purification, retaining robust *in vitro* radiostability after 48 h incubation. *In vivo* biodistribution assays in mice showed that ^{131}I-EVs^{ABPC} predominantly accumulated in the lungs, heart, liver and kidneys at early time points, followed by rapid, time-dependent whole-body clearance. Pharmacokinetic modeling identified the three-compartment and two-compartment models as the optimal fits for mice and macaques, respectively; circulating half-lives were markedly extended in non-human primates. Cross-species SPECT/CT imaging revealed consistent hepatic, pulmonary and renal uptake in both species, while gradual tracer accumulation in the thyroid and gastrointestinal tract stemmed mainly from *in vivo* deiodination. Notably, distinct uptake signals in bone and nasal mucosa underscore the promising translational value of EVs^{ABPC} for targeted treatment of nasopharyngeal carcinoma and orthopedic diseases.

Conclusions

This study realized non-invasive *in vivo* visualization and quantitative biodistribution profiling of EVs^{ABPC}. These comprehensive cross-species imaging and pharmacokinetic data provide solid, objective preclinical evidence to accelerate the clinical translation of EVs^{ABPC}-based therapeutics and underpin future clinical research on EVs delivery platforms.

Introduction

Extracellular vesicles (EVs) are membrane-bound vesicles released by cells into the extracellular microenvironment[1–3]. Functionally, they orchestrate intercellular communication, cell migration and angiogenesis, and modulate tumor cell proliferation[4–6]. Mounting evidence has established their central roles in the onset and progression of diverse pathological disorders, rendering EVs powerful candidate biomarkers for disease screening and diagnosis[7]. Meanwhile, owing to their intrinsic lipid bilayer structure, low immunogenicity and natural tissue-targeting trafficking ability, EVs have garnered extensive research attention as versatile nanocarriers for drug delivery[8–9]. Although multiple EV-based therapeutic candidates have progressed to clinical trials, the translational advancement of EV therapeutics is still impeded by substantial technical and translational barriers[10–13].

The clinical translation of EV-based therapeutics is hindered by a major bottleneck: standardized protocols for systematic characterization of EV *in vivo* pharmacokinetics and biosafety remain lacking[14]. There is an urgent demand for whole-body, real-time, dynamic and quantitative tracking of EVs in living subjects[15]. Optical imaging is conventionally adopted for EV investigations yet plagued by frequent false-positive artifacts[16–17]. In contrast, nuclear medicine imaging exhibits unique strengths, including exceptional detection sensitivity, deep tissue penetration, reliable quantitative outputs and excellent targeting capacity, which qualifies it as the preferred modality for *in vivo* EV imaging[18–21]. Iodine radionuclides are capable of direct conjugation to EV membranes. This labeling approach circumvents additional chemical derivatization, simplifies experimental procedures, and preserves the structural integrity of EV membranes, thereby establishing a robust technical platform for the *in vivo* visualization and functional evaluation of EVs[22–23].

We previously isolated a distinctive subpopulation of skeletal mesenchymal stem cells termed antler blastema progenitor cells (ABPCs)[24]. ABPC-derived secretory vesicles ameliorate motor and cognitive performance, confer neuroprotective effects, and mitigate systemic inflammation, paving a novel path for EV-targeted anti-senescence therapeutics[25]. In the present study, to elucidate the in vivo biodistribution and kinetic profiles of EVs^{ABPC} and conduct cross-species biodistribution comparisons between mice and macaques with markedly divergent physiological sizes, we adopted EVs^{ABPC} as the research platform and leveraged nuclear molecular imaging to perform comprehensive, dynamic, non-invasive *in vivo* tracing. Collectively, this investigation establishes a practical framework for the development and preclinical assessment of EV-based therapeutic strategies, thereby expediting their translation to clinical practice.

Experimental section

General method

All chemicals and solvents were purchased from commercial suppliers and used without further purification. [^{131}I]NaI was obtained from HTA Co., Ltd. (Beijing, China). Iodogen was acquired from Sigma-Aldrich LLC. A Mini-Scan radio-TLC Scanner (BioScan, USA) was employed to assess the labeling efficiency and radiochemical purity, while radioactivity measurements were performed using a γ-counter (WIZARD 2470, PerkinElmer, USA). For SPECT/CT imaging, a micro-SPECT/CT scanner (U-SPECT, MILabs, Netherlands) and a SPECT/CT scanner (Discovery NM/CT 670, GE Healthcare, USA) were utilized for mice and healthy macaques, respectively.

Preparation of EVs

ABPCs were obtained from the pedicle periosteum of 2-year-old male sika deer 5 days after antler casting. The deer received 3 mg/kg xylazine via hind-limb intramuscular injection for anaesthesia. After sterilization of the pedicle region, an incision was performed to expose the pedicle periosteum and regenerating antler tissue. The pedicle periosteum was harvested. Upon haemostasis, an equivalent intravenous dose of idazoxan hydrochloride was administered to reverse xylazine-induced anaesthesia. The pedicle periosteum was harvested and immersed in minimum essential medium α (MEM α) for downstream processing. A total of 2.5 × 10^7 sorted cells were seeded into 3D spinner flasks and cultured in complete medium supplemented with extracellular vesicle-depleted fetal bovine serum (EV-free FBS). Cell culture supernatants underwent serial centrifugation at 4°C for the isolation of ABPC-derived extracellular vesicles EVs^{ABPC}. The purified EVs^{ABPC} were resuspended in phosphate-buffered saline (PBS) to a final concentration of 2 μg/μL, divided into aliquots, and stored at -80°C for subsequent experiments. Transmission electron microscopy (TEM) with negative staining was utilized to characterize the morphology of EVs^{ABPC} at 80.0 kV with a magnification of ×280,000.

Radiochemistry

EVs^{ABPC} were radiolabeled with ^{131}I using Iodogen as the oxidizing agent. Briefly, 50 μL of EVs^{ABPC} and [^{131}I]NaI solution (2 mL, 10 mCi) were sequentially added to EP tubes pre-coated with 20 μg Iodogen. The labeling reaction was carried out for 10 min at 37°C. A 3 μL aliquot of the reaction mixture was withdrawn to determine the radiolabeling efficiency by ITLC-SG paper chromatography with normal saline as the mobile phase. The remaining crude reaction mixture was purified using a PD-10 desalting column, followed by sterile filtration through a 0.22 μm Millex-GS filter. The post-purification eluate was collected for quantification of the radiochemical purity of the final ^{131}I-EVs^{ABPC} product.

For *in vitro* stability assessment, ^{131}I-EVs^{ABPC} was diluted with normal saline and mouse serum separately, and incubated at 37°C for 48 h. The radiochemical stability of the ^{131}I-EVs^{ABPC} probe was

finally verified by ITLC analysis after the incubation period.

Biodistribution and pharmacokinetics studies in mice

Male ICR mice were randomly divided into seven groups (n = 5) and given an intravenous injection of 0.1 mL normal saline containing ^{131}I-EVs^{ABPC} (0.72 MBq). Mice were deeply anesthetized with isoflurane (confirmed by loss of the pedal withdrawal reflex) and then euthanized by decapitation at 0.25, 1, 4, 8, 24, 96, and 192 hours post-injection (p.i.). Blood samples were collected, and major organs including the brain, heart, liver, spleen, lung, kidney, bone, muscle, small intestine, stomach, and tail were surgically excised. After weighing each organ, radioactivity levels were measured with a gamma counter, followed by the calculation of the percentage injected dose per gram wet weight (% ID/g).

Fittings of various compartment models with distinct weighting factors were carried out using the PKSlover pharmacokinetic software to identify the optimal model[26–27].

Micro-SPECT/CT imaging in mice

Micro-SPECT/CT imaging was performed in healthy ICR mice. Three days before imaging, four mice received daily intragastric administration of 20 μL Lugol's solution (5% I_2 mass fraction) to block thyroidal uptake of free ^{131}I. Thereafter, each mouse was intravenously injected via the tail vein with 200 μL of ^{131}I-EVsABPC containing an activity of 18.5 MBq. Mice were maintained under isoflurane anesthesia (2% in air, 1.5 L/min) and subjected to sequential Micro-SPECT/CT scans at 1, 4, 8, 24, 96, and 192 h p.i.. Imaging was acquired using a high-energy mouse collimator equipped with a 3.6 mm-diameter pinhole aperture. The collimator possessed a central field of view with a diameter of approximately 28 mm and an axial length of 18 mm.

All SPECT and CT datasets were reconstructed and co-registered using the manufacturer-supplied software. SPECT images were reconstructed into 0.8 mm cubic voxels with a 20% photopeak energy window centered at 364 keV. A total of six iterations with 128 subsets were applied for reconstruction across all scans. Two contiguous background and scatter correction windows (each approximately 5% energy width) were adopted for Compton scatter and background signal subtraction via the triple-energy window algorithm.

SPECT imaging in healthy macaque

Before SPECT/CT acquisition, macaque received oral administration of 0.5 mL Lugol's solution (5% I_2 mass fraction) once daily for three consecutive days for thyroid blockade. After this pretreatment, the monkey was anesthetized with propofol, followed by intravenous injection of ^{131}I-EVs^{ABPC} (37.0 MBq). Planar SPECT and quantitative SPECT/CT scans were acquired at 1, 4 and 8 hours p.i.. Imaging was conducted on a dual-head γ-camera fitted with a high-energy general-purpose collimator. CT acquisition was performed subsequent to SPECT scanning to allow image co-registration and fusion of SPECT

functional data with CT anatomical data. After full dataset reconstruction, regions of interest (ROIs) were manually delineated on target organs (OIs) at each time point, and the mean standardized uptake values (SUVs) of individual organs were calculated. After the experiment, the macaque was returned to the non-human primate housing area and provided with routine husbandry and health monitoring.

Dosimetric Study in Adult Phantoms

To determine the organ residence times of ^{131}I-EVsABPC in male ICR mice and healthy macaques, dosimetric calculations and statistical analyses were performed using GraphPad Prism software. Referencing previously published protocols and adopting the organ mass parameters from the adult male phantom embedded in OLINDA/EXM software, the organ residence times obtained from mice and macaque were converted into equivalent residence times of the corresponding source organs in a 73.4 kg standard adult male phantom[28]. Finally, the analytical modules of OLINDA/EXM were applied to calculate the organ-specific effective dose (ED) and effective dose equivalent (EDE) values for the reference adult male phantom.

Statistical analysis

All data are expressed as mean ± standard deviation (SD). All statistical analyses were performed with GraphPad Prism 9.0 (GraphPad, Chicago, IL, USA). Differences between two groups were determined using Student's *t*-tests. One-way ANOVA was used for comparing among groups. *P*-values are expressed as: * $p < 0.05$, ** $p < 0.01$, and *** $p < 0.001$.

ARRIVE guidelines

The work has been reported in line with the ARRIVE guidelines 2.0.

Results

Radiochemistry

Typical cup-shaped EVs with intact lipid bilayer membranes were visualized, with diameters ranging from 100 nm to 160 nm, consistent with the size range of microvesicles and large exosomes (Fig. 1A). Subsequently, we successfully prepared ^{131}I-EVs^{ABPC}, as shown **in** Fig. 1B. Upon completion of the labeling reaction at 37°C, an aliquot of the reaction mixture was analyzed via iTLC. The results demonstrated that the radiochemical yield (RCY) of the ^{131}I-EVs^{ABPC} probe reached 67.6% (Fig. 1C). After purification, the radiochemical purity (RCP) of the radiolabeled product reached over 99%. Collectively, these data confirmed that high-purity radiolabeled probes can be readily obtained via straightforward purification after the 37°C labeling reaction. Furthermore, ^{131}I-EVs^{ABPC} displayed favorable *in vitro* stability. After 48 h of incubation in normal saline and serum, the RCP of ^{131}I-EVs^{ABPC} declined slightly to 96.3% and 91.7%, respectively. These results lay the groundwork for future *in vivo* imaging studies.

Biodistribution in male ICR mice

As presented in Fig. 2A, the *in vivo* biodistribution profile of ^{131}I-EVs^{ABPC} was consistent with that of typical EVs. Biodistribution data demonstrated that ^{131}I-EVs^{ABPC} mainly resided in the circulatory system at early time points. The radioactivity in blood reached a maximum of 21.49 ± 0.97% ID/g at 15 min p.i. Following the peak, the tracer underwent sustained rapid elimination across the observation interval, and 88.2% clearance was achieved within 24 h p.i. At 96 h p.i., nearly complete clearance from the bloodstream was noted, with residual radioactivity falling to 0.20 ± 0.04% ID/g. ^{131}I-EVs^{ABPC} accumulated extensively in the lungs (10.44 ± 1.40% ID/g) and distributed moderately within the heart, liver, spleen and kidneys (approximately 5% ID/g) at 15 min p.i. These organs exhibited time-dependent clearance kinetics comparable to those seen in the blood; by 24 h p.i., over 80% of the tracer had been eliminated from these tissues. In addition, substantial tracer accumulation was detected in the intestines, which displayed an initial rise followed by a gradual decline, with peak uptake of 7.81 ± 1.37% ID/g attained at 1 h p.i.

Pharmacokinetics in Male ICR Mice

Calculations performed via the PKSolver pharmacokinetic software provided the theoretical basis for selecting the atrial hemodynamic model. With the weighting factor set to 1/cc, the three-compartment model achieved the minimum Akaike Information Criterion (AIC) and Schwarz Criterion (SC) values, suggesting optimal consistency with the *in vivo* metabolic profile of the probe. Figure 2B displays the blood time-concentration curve. After tail vein administration, blood concentrations rose rapidly to a peak. The distribution half-life ($T_{1/2}\alpha$) and elimination half-life ($T_{1/2}\beta$) were 2.476 h and 16.69 h, respectively.

Small Animal Micro-SPECT/CT Imaging

We further performed whole-body dynamic tracing of ^{131}I-EVs^{ABPC} via micro-SPECT/CT imaging to elucidate its *in vivo* biodistribution and kinetic characteristics. Figure 2c shows a typical image of one of the mice. The thyroid gland was blocked with Lugol's solution prior to imaging. Thyroid radioiodine uptake was almost completely suppressed within 24 h p.i., whereas prominent radioactivity accumulation was observed in the thyroid at 4 d p.i., indicating deiodination of ^{131}I-EVs^{ABPC}. In addition, intense radioactivity was detected in the stomach within 24 h p.i., further verifying the occurrence of *in vivo* deiodination. The gastric radioactivity was metabolized and transferred to the intestine by 24 h p.i., followed by excretion from the body. Virtually no radioactivity was detectable in the gastrointestinal tract at 96 h p.i. For other organs, prominent cardiac radioactivity accumulation was observed at the initial time of 1 h and 4 h p.i., which was rapidly cleared over time. The liver was another organ with obvious radioactive signals on micro-SPECT/CT images.

SPECT Imaging in Healthy macaque

As shown in Fig. 3, first-in-macaque SPECT/CT imaging of ^{131}I-EVs^{ABPC} was conducted in this study. The *in vivo* biodistribution profiles obtained from macaques were highly consistent with those derived from mouse experiments. Planar SPECT images revealed intense radioactivity sequestration in the liver and cardiac blood pool. Quantitative SPECT/CT analysis demonstrated that cardiac SUVmax reached 6.83 at 1 h p.i. Although cardiac SUVmax decreased progressively over time, a measurable value of 4.21 remained detectable at 8 h p.i. Overall, ^{131}I-EVs^{ABPC} exhibited widespread uptake in key organs including the liver, lungs, and kidneys, with SUVmax values of 4.96, 4.27, and 3.29 at 1 h p.i. Radioactivity signals gradually diminished in most tissues. In contrast, SUVmax values of the spleen, stomach, and small intestine increased continuously, peaking at 3.27, 5.81, and 2.24 at 8 h p.i., respectively. Similar to the mouse studies, Lugol's solution was pre-administered to block thyroid iodine uptake in macaques; no obvious radioiodine sequestration was identified in the thyroid gland within the first 8 h p.i. Additionally, distinct uptake signals of ^{131}I-EVs^{ABPC} were visualized in the nasal cavities of macaques, displaying an early rising trend followed by a gradual decrease.

Radioanalysis of blood from healthy macaques

Quantification of blood radioactivity revealed peak circulating levels of ^{131}I-EVs^{ABPC} at 30 min p.i., followed by rapid systemic clearance, during which blood radioactivity dropped by 30% over the next 30 min. Clearance slowed significantly after 60 min, and radioactivity plateaued at approximately 0.012% ID/mL from 60 to 480 min. As shown in Fig. 4A, the radiotracer was predominantly distributed in plasma with minimal binding to blood cells. Pharmacokinetic analysis using PKSlover software confirmed that the two-compartment model (weighting factor = 1) provided the optimal fit for the in vivo kinetic profiles of ^{131}I-EVs^{ABPC} in macaques (Fig. 4B). Compared with mice, ^{131}I-EVs^{ABPC} exhibited markedly longer distribution half-lives ($T_{1/2}\alpha$ = 39.26 h) and terminal elimination half-lives ($T_{1/2}\beta$ = 2187 h) in macaques.

Dosimetry

As summarized in Table 1, dosimetric calculations for adult anthropomorphic phantoms extrapolated from murine biodistribution data show strong concordance with quantitative SPECT/CT imaging measurements acquired in macaques. ^{131}I-EVs^{ABPC} exhibited lower Effective Dose Equivalent (EDE) and Effective Dose (ED) in both adult phantoms. Radiosensitive organs, such as red bone marrow and testes, received negligible absorbed doses, which corroborates the excellent radiological safety of this radiotracer. Consistent with the intrinsic biodistribution profile of ^{131}I-EVs^{ABPC}, the spleen, liver, cardiac wall, kidneys, and lungs bore the highest radiation burdens, with absorbed doses ranging from 10.5 to 69.0 μGy·MBq^{-1} across all adult phantoms. Prophylactic administration of Lugol's solution effectively inhibited thyroidal radiotracer accumulation, restricting the thyroid absorbed dose to less than 1.0 μGy·MBq^{-1} in all phantom simulations.

Table 1

Estimates of human organ absorbed radiation dosimetry of ^{131}I-EVs^{ABPC} with adult phantoms.

Target Organ [a]	**Adult phantoms 1 (μGy·MBq^{-1})** [b]	**Adult phantoms 2 (μGy·MBq^{-1})** [c]
Adrenals	4.47	3.72
Brain	5.86	4.47
Breasts	2.00	1.03
Gallbladder Wall	5.66	5.55
LLI Wall	2.06	0.18
Small Intestine	46.7	0.91
Stomach Wall	8.13	1.97
ULI Wall	5.52	1.32
Heart Wall	38.7	46.8
Kidneys	44.5	13.5
Liver	32.0	47.8
Lung	69.0	10.5
Muscle	1.46	0.79
Ovaries	3.16	0.34
Pancreas	4.33	3.95
Red Marrow	2.02	0.97
Osteogenic Cells	1.51	0.84
Skin	0.68	0.41
Spleen	26.2	58.6
Testes	0.14	0.03
Thymus	2.54	1.45

[a] LLI is Lower large intestine, ULI is Upper large intestine, EDE is Effective Dose Equivalent, and ED is Effective Dose.

[b] Based on the results of biodistribution in mice.

[c] Based on the results of SPECT/CT quantitative imaging in macaque.

Target Organ [a]	Adult phantoms 1 (μGy·MBq^{-1}) [b]	Adult phantoms 2 (μGy·MBq^{-1}) [c]
Thyroid	0.70	0.27
Urinary Bladder Wall	0.79	0.14
Uterus	2.78	0.29
Total body	4.09	2.60
EDE (μSv·MBq^{-1})	21.0	12.0
EDE (μSv·MBq^{-1})	12.9	5.72

[a] LLI is Lower large intestine, ULI is Upper large intestine, EDE is Effective Dose Equivalent, and ED is Effective Dose.

[b] Based on the results of biodistribution in mice.

[c] Based on the results of SPECT/CT quantitative imaging in macaque.

Discussion

Herein, EVs^{ABPC} were radiolabeled with ^{131}I. A systematic assessment of their *in vivo* pharmacokinetic profiles and whole-body biodistribution was conducted. In parallel, *in vivo* SPECT/CT imaging was implemented in non-human primate macaques to delineate the systemic trafficking behavior of the EVs-derived vesicles. Notably, this work reports the first *in vivo* primate imaging dataset for EVs-targeted nuclear molecular imaging.

In mice, ^{131}I-EVs^{ABPC} preferentially accumulated within the lungs and liver. By contrast, macaque SPECT/CT revealed sustained high radiotracer signals in the lungs and liver, alongside prominent cardiac retention. Such interspecies discrepancy could be attributed to body-size-dependent disparities in basal metabolism[29], a finding aligned with the markedly prolonged circulatory and elimination half-lives measured in macaques relative to mice. Furthermore, SUVs within the spleen, stomach, and small intestine rose progressively across all imaging time points. This biodistribution pattern agreed with published data demonstrating the physiological tropism of EVs for the liver, spleen, gastrointestinal tracts, and lungs. Our findings also corroborated prior studies regarding administration route-dependent EVs trafficking: intravenously administered EVs predominantly accumulated in the pulmonary, hepatic and splenic tissues[30].

Strong radiotracer accumulation in the stomach was visualized on serial SPECT images acquired from both mice and macaques. In macaques, the gastric SUV peaked at 5.81 at 8 h p.i. Notably, stomach specimens collected for murine ex vivo biodistribution assays were emptied of luminal contents prior to

radioactivity quantification, resulting in markedly lower gastric retention, with a maximal uptake of only 2.18 ± 0.29% ID/g at 1 h p.i. Collectively, these findings demonstrate that gastric radioactivity originates from both gastric parenchymal tissue and intraluminal contents. ^{131}I-EVs^{ABPC} undergoes progressive in vivo deiodination. The basolateral membrane of gastric parietal cells abundantly expresses the sodium–iodide symporter (NIS), which mediates iodide uptake through a molecular pathway identical to that of thyroid follicular cells[31]. This transporter actively shuttles free $^{131}I^-$ from systemic circulation against concentration gradients into the gastric mucosa and luminal fluid, thereby producing persistently high gastric radioactivity. Meanwhile, intact EVs are predominantly sequestered and metabolized within the liver and spleen. The resulting radiometabolites are secreted into the gastrointestinal tract via biliary excretion, further amplifying this transient physiological gastric tracer signal.

EVs possess intrinsic tumor-homing capacity and stand out as promising natural nanocarriers for targeted drug delivery[32]. The present study validated that EVs^{ABPC} constitute a viable therapeutic platform for nasopharyngeal carcinoma (NPC). Distinct nasal mucosal radiotracer retention was readily detectable on macaque SPECT/CT scans. Attributable to the inherent mucoadhesive characteristics of the exosomal lipid bilayer, intravenously administered EVs extravasate across the vascular endothelium into the nasal submucosa, where they adhere to the mucus coating lining olfactory and respiratory epithelia. Such favorable nasal mucosal accumulation unlocks a unique opportunity for localized NPC intervention. In addition, nasal respiratory epithelial cells express low levels of the NIS[33], which mediates mild sequestration of dissociated free $^{131}I^-$ and partially contributes to the nasal radioactive signal. Collectively, ^{131}I-radiolabeled EVs^{ABPC} represent an innovative alternative for NPC radionuclide targeted therapy, complementing existing SSTR- and FAP-targeted probes radiolabeled with ^{177}Lu[34–35].

EVs-based therapeutics have emerged as a promising modality for treating a variety of orthopedic degenerative disorders[25]. ABPCs are unique skeletal mesenchymal stem cells originating from regenerating deer antlers, which possess prominent stemness properties and potent self-renewal capacity *in vitro*. Our previous studies have verified that EVs^{ABPC} effectively ameliorate senescent phenotypes in bone marrow stem cells. *In vivo*, EVs^{ABPC} intervention markedly enhances femoral bone mineral density in aged mice and macaques. In line with these favorable therapeutic outcomes, our current cross-species biodistribution data further confirm persistent high accumulation of ^{131}I-EVs^{ABPC} in osseous tissues of both mice and macaques. Such a desirable bone-targeting distribution profile solidifies preclinical evidence for the translational potential of EVs^{ABPC}, supporting their further clinical development for orthopedic disease therapy.

EVs^{ABPC} confer potent anti-senescent benefits in a wide range of tissues, with particularly striking protective activity within the central nervous system[25]. In aged mice, EVs^{ABPC} reversed age-associated cognitive deterioration and alleviated anxiety-like behavioral phenotypes. In aged rhesus macaques, prolonged systemic EVs^{ABPC} treatment triggered robust anti-aging responses in the brain and induced significant expansion of cerebral cortical volume. Despite these encouraging neuroprotective outcomes,

quantitative analysis uncovered limited brain uptake of ^{131}I-EVs^{ABPC}. Peak brain uptake in mice reached 0.51 ± 0.15% ID/g at 15 min p.i., whereas the SUV_{avg} remained below 0.4 in macaques. Collectively, these observations confirm that unmodified EVs^{ABPC} exhibit intrinsically poor permeability across the blood-brain barrier (BBB). Future investigations will center on surface engineering of EVs^{ABPC} to improve cerebral delivery efficiency, thereby enhancing their therapeutic efficacy against age-related cerebral senescence[36].

EVs act as core vehicles mediating intercellular signaling and serve as endogenous biological couriers for targeted delivery of cellular cargo. They possess prominent research prospects and translational value in physiological modulation, disease diagnosis, and targeted drug delivery. Advances in automated manufacturing, AI-driven process optimization, and harmonized regulatory guidelines will streamline EVs fabrication and expand clinical access to these vesicle therapeutics. Meanwhile, nuclear molecular imaging, featuring unique real-time, dynamic, quantitative, and non-invasive imaging capability, will substantially accelerate preclinical screening, therapeutic efficacy evaluation, and the translational advancement of EVs-based treatments.

Conclusion

Cross-species SPECT/CT imaging verified ^{131}I radiolabeling as a reliable strategy for non-invasive in vivo tracking of EVsABPC. Biodistribution quantification revealed marked bone tropism yet weak cerebral permeation of unmodified ^{131}I-EVs^{ABPC} in mice and macaques. Collectively, this work confirms the therapeutic promise of EVs^{ABPC} for orthopedic and cerebral degenerative diseases and validates ^{131}I radionuclide tracing for assessing EV biodistribution. These cross-species quantitative imaging data supply unbiased preclinical evidence to accelerate the clinical translation of EV therapeutics.

Associated content

The biodistribution of ^{131}I-EVs^{ABPC} in male ICR mice, rationale for selection of hemodynamic chamber model, biodistribution of ^{131}I-EVs^{ABPC} in macaque and MIP of heathy macaque can be found in the Supporting Information.

Ethics approval

All animal procedures complied with the Association for Assessment and Accreditation of Laboratory Animal Care International (AAALAC International) guidelines. The sika deer experiment for antler blastema progenitor cell harvesting was approved by the Animal Ethics Committee of Changchun Sci-Tech University (Approval No. CKARI202007, approved in 2020). The animal study on the anti-aging effects of EVs in macaques and mice was approved by the Animal Ethics Committee of the Fourth Military Medical University on April 5, 2023 (Approval No. IACUC-20230075). Mice were housed in SPF cages under a 12 h light–dark cycle at 22 ± 2°C and 50 ± 10% humidity, with bedding and nesting material

provided for environmental enrichment. Macaques were housed in standard non-human primate cages with foraging enrichment toys.

Declarations

Associated content

The biodistribution of ^{131}I-EVs^{ABPC} in male ICR mice, rationale for selection of hemodynamic chamber model, biodistribution of ^{131}I-EVs^{ABPC} in macaque and MIP of heathy macaque can be found in the Supporting Information.

Ethics approval

All animal procedures complied with the Association for Assessment and Accreditation of Laboratory Animal Care International (AAALAC International) guidelines. The sika deer experiment for antler blastema progenitor cell harvesting was approved by the Animal Ethics Committee of Changchun Sci-Tech University (Approval No. CKARI202007, approved in 2020). The animal study on the anti-aging effects of EVs in macaques and mice was approved by the Animal Ethics Committee of the Fourth Military Medical University on April 5, 2023 (Approval No. IACUC-20230075). Mice were housed in SPF cages under a 12 h light–dark cycle at 22 ± 2 °C and 50 ± 10% humidity, with bedding and nesting material provided for environmental enrichment. Macaques were housed in standard non-human primate cages with foraging enrichment toys.

Funding

We acknowledge the financial support from the Shaanxi Province Key Industry Innovation Chain (2024SF-ZDCYL-02-06) and National Natural Science Foundation of China (82402323, 92259304).

Declaration of Competing Interest

The authors declare that they have no known competing financial interests or personal relationships that could have appeared to influence the work reported in this paper.

AUTHOR INFORMATION

Corresponding Authors

Fei Kang - Department of Nuclear Medicine, Xijing Hospital, Fourth Military Medical University, Xi'an, Shaanxi, 710032, China. Email: fmmukangf@fmmu.edu.cn.

Jing Wang - Department of Nuclear Medicine, Xijing Hospital, Fourth Military Medical University, Xi'an, Shaanxi, 710032, China. Email: 13909245902@163.com.

Jinghui Huang - Department of Orthopedics, Xijing Hospital, Fourth Military Medical University, Xi'an, Shaanxi, 710032, China. Email:huangjh@fmmu.edu.cn.

Authors

Jiajun Ye - Department of Nuclear Medicine, Xijing Hospital, Fourth Military Medical University, Xi'an, Shaanxi, 710032, China

Kangxia Yu - Department of Nuclear Medicine, Xijing Hospital, Fourth Military Medical University, Xi'an, Shaanxi, 710032, China

Chen Zhou - Department of Nuclear Medicine, Xijing Hospital, Fourth Military Medical University, Xi'an, Shaanxi, 710032, China

Yiming Hao - Department of Orthopedics, Xijing Hospital, Fourth Military Medical University, Xi'an, Shaanxi, 710032, China

Guoquan Li - Department of Nuclear Medicine, Xijing Hospital, Fourth Military Medical University, Xi'an, Shaanxi, 710032, China

Xiaoyan Liang - Department of Nuclear Medicine, Xijing Hospital, Fourth Military Medical University, Xi'an, Shaanxi, 710032, China

Guiyu Li - Department of Nuclear Medicine, Xijing Hospital, Fourth Military Medical University, Xi'an, Shaanxi, 710032, China

Zifan Zhu - Department of Nuclear Medicine, Xijing Hospital, Fourth Military Medical University, Xi'an, Shaanxi, 710032, China

Cai Xu - Department of Nuclear Medicine, Xijing Hospital, Fourth Military Medical University, Xi'an, Shaanxi, 710032, China

Pengan Xiang - Department of Nuclear Medicine, Xijing Hospital, Fourth Military Medical University, Xi'an, Shaanxi, 710032, China

Author Contributions

#J.Y., K.Y. and C.Z. contributed equally to this work. J.Y.: Writing original draft, Investigation, Data curation, Funding acquisition. K.Y. and C.Z.: Validation, Investigation. Y.H., G.L., X.L., G.L., Z.Z., C.X., and P.X.: Validation, Methodology. J.H., J.W., and F.K.: Writing review and editing, Supervision, Funding acquisition, Project administration, Conceptualization.

Data Availability

All study data are included in the manuscript and Supplementary Information.

AI

The authors declare that they have not used AI-generated content in this manuscript.

Acknowledgment

We thank Dr. Li Zhipeng from the Institute of Antler Science and Product Technology, Changchun Sci-Tech University, our partner institute, for antler collection.

References

1. Fusco C, De Rosa G, Spatocco I, Vitiello E, Procaccini C, Frigè C et al (2024) Extracellular vesicles as human therapeutics: A scoping review of the literature. J Extracell Vesicles 13(5):e12433
2. Ma Y, Brocchini S, Williams GR (2023) Extracellular vesicle-embedded materials. J Control Release 361:280–296
3. Zhou X, Huang J, Zhang D, Qian Z, Zuo X, Sun Y (2025) Small extracellular vesicles: the origins, current status, future prospects, and applications. Stem Cell Res Ther 16(1):184
4. Colombo M, Raposo G, Théry C (2014) Biogenesis, secretion, and intercellular interactions of exosomes and other extracellular vesicles. Annu Rev Cell Dev Biol 30:255–289
5. Ludwig AK, Giebel B (2012) Exosomes: small vesicles participating in intercellular communication. Int J Biochem Cell Biol 44(1):11–15
6. Welsh JA, Goberdhan D, O'Driscoll L, Buzas EI, Blenkiron C, Bussolati B et al (2024) Minimal information for studies of extracellular vesicles (MISEV2023): From basic to advanced approaches. J Extracell Vesicles 13(2):e12404
7. Tsering T, Nadeau A, Wu T, Dickinson K, Burnier JV (2024) Extracellular vesicle-associated DNA: ten years since its discovery in human blood. Cell Death Dis 15(9):668
8. Rohm TV, Cunha ERK, Olefsky JM (2025) Metabolic Messengers: small extracellular vesicles. Nat Metab 7(2):253–262
9. Wang J, Yin B, Lian J, Wang X Extracellular Vesicles as Drug Delivery System for Cancer Therapy. Pharmaceutics, 2024,16(8).
10. Brancolini A, Vago R Investigating the Potential of Extracellular Vesicles as Delivery Systems for Chemotherapeutics. Biomedicines, 2024,12(12)
11. Ou YH, Liang J, Czarny B, Wacker MG, Yu V, Wang JW et al (2021) Extracellular Vesicle (EV) biohybrid systems for cancer therapy: Recent advances and future perspectives. Semin Cancer Biol 74:45–61
12. Zhang LY, Yang X, Wang SB, Chen H, Pan HY, Hu ZM (2020) Membrane Derived Vesicles as Biomimetic Carriers for Targeted Drug Delivery System. Curr Top Med Chem 20(27):2472–2492
13. Ming-Kun C, Zi-Xian C, Mao-Ping C, Hong C, Zhuang-Fei C, Shan-Chao Z (2024) Engineered extracellular vesicles: A new approach for targeted therapy of tumors and overcoming drug

resistance. Cancer Commun (Lond) 44(2):205–225

14. Panagopoulou MS, Wark AW, Birch D, Gregory CD (2020) Phenotypic analysis of extracellular vesicles: a review on the applications of fluorescence. J Extracell Vesicles 9(1):1710020
15. Gangadaran P, Hong CM, Ahn BC (2017) Current Perspectives on In Vivo Noninvasive Tracking of Extracellular Vesicles with Molecular Imaging. Biomed Res Int 2017:9158319
16. Ma B, Li L, Bao Y, Yuan L, Liu S, Qi L et al (2024) Optical Imaging of Single Extracellular Vesicles: Recent Progress and Prospects. Chem Biomed Imaging 2(1):27–46
17. Guo J, Zhu Y, Qu Y, Zhang L, Fang M, Xu Z et al (2024) Structure Tailoring of Hemicyanine Dyes for In Vivo Shortwave Infrared Imaging. J Med Chem 67(18):16820–16834
18. Mohan AM, Beindorff N, Brenner W (2021) Nuclear Medicine Imaging Procedures in Oncology. Methods Mol Biol 2294:297–323
19. Khan AA, T M D R (2021) R. Radiolabelling of Extracellular Vesicles for PET and SPECT imaging. Nanotheranostics 5(3):256–274
20. Arifin DR, Witwer KW, Bulte J (2022) Non-Invasive imaging of extracellular vesicles: Quo vaditis in vivo? J Extracell Vesicles 11(7):e12241
21. Jung KO, Kim YH, Chung SJ, Lee CH, Rhee S, Pratx G et al Identification of Lymphatic and Hematogenous Routes of Rapidly Labeled Radioactive and Fluorescent Exosomes through Highly Sensitive Multimodal Imaging. Int J Mol Sci, 2020,21(21).
22. Patel S, Schmidt KF, Farhoud M, Zi T, Jang SC, Dooley K et al (2022) In vivo tracking of [(89)Zr]Zr-labeled engineered extracellular vesicles by PET reveals organ-specific biodistribution based upon the route of administration. Nucl Med Biol 112–113:20–30
23. Yang CT, Lai RC, Phua V, Aw SE, Zhang B, Sim WK et al Standard Radio-Iodine Labeling Protocols Impaired the Functional Integrity of Mesenchymal Stem/Stromal Cell Exosomes. Int J Mol Sci, 2024,25(7).
24. Qin T, Zhang G, Zheng Y, Li S, Yuan Y, Li Q et al (2023) A population of stem cells with strong regenerative potential discovered in deer antlers. Science 379(6634):840–847
25. Hao Y, Yu B, Qin M, Qin T, Wang J, Wei Y et al (2025) Extracellular vesicles from antler blastema progenitor cells reverse bone loss and mitigate aging-related phenotypes in mice and macaques. Nat Aging 5(9):1790–1809
26. Ye J, Yang W, Xie Z, Yan Y, Li G, Li G et al (2023) Safety, Biodistribution, and Dosimetry Study of Meplazumab, a Potential COVID-19 Therapeutic Drug, with 131I-Labeling and SPECT Imaging. Mol Pharm 20(3):1750–1757
27. Ye J, Yang S, Liu Y, Quan Z, Zhang M, Li G et al (2025) Pharmacokinetics study of FT-FAPI, a novel multi-nuclide label-able FAP targeting tracer, in mice and healthy volunteers. Eur J Nucl Med Mol Imaging 52(13):4939–4951
28. Stabin MG, Sparks RB, Crowe E (2005) OLINDA/EXM: The Second-Generation Personal Computer Software for Internal Dose Assessment in Nuclear Medicine. J Nucl Med 46(6):1023

29. Grula CC, Rinehart JP, Greenlee KJ, Bowsher JH (2021) Body size allometry impacts flight-related morphology and metabolic rates in the solitary bee Megachile rotundata. J Insect Physiol 133:104275
30. Driedonks T, Jiang L, Carlson B, Han Z, Liu G, Queen SE et al (2022) Pharmacokinetics and biodistribution of extracellular vesicles administered intravenously and intranasally to Macaca nemestrina. J Extracell Biol, 1(10)
31. Josefsson M, Grunditz T, Ohlsson T, Ekblad E (2002) Sodium/iodide-symporter: distribution in different mammals and role in entero-thyroid circulation of iodide. Acta Physiol Scand 175(2):129–137
32. Liang T, Chen L, Liu X, Li Y, Li Z, Yang D et al (2023) The role of extracellular vesicles in the development of nasopharyngeal carcinoma and potential clinical applications. Cancer Med 12(13):14484–14497
33. Morgenstern KE, Vadysirisack DD, Zhang Z, Cahill KV, Foster JA, Burns JA et al (2005) Expression of sodium iodide symporter in the lacrimal drainage system: implication for the mechanism underlying nasolacrimal duct obstruction in I(131)-treated patients. Ophthalmic Plast Reconstr Surg 21(5):337–344
34. Chen J, Pang Y, Liao X, Zhou Y, Luo Q, Wu H et al (2024) Development of [(177)Lu]Lu-LNC1010 for peptide receptor radionuclide therapy of nasopharyngeal carcinoma. Eur J Nucl Med Mol Imaging 52(1):247–259
35. Fu K, Pang Y, Zhao L, Lin L, Wu H, Sun L et al (2022) FAP-targeted radionuclide therapy with [(177)Lu]Lu-FAPI-46 in metastatic nasopharyngeal carcinoma. Eur J Nucl Med Mol Imaging 49(5):1767–1769
36. Zhu Y, Huang R, Wang D, Yu L, Liu Y, Huang R et al (2023) EVs-mediated delivery of CB2 receptor agonist for Alzheimer's disease therapy. Asian J Pharm Sci 18(4):100835

Figures

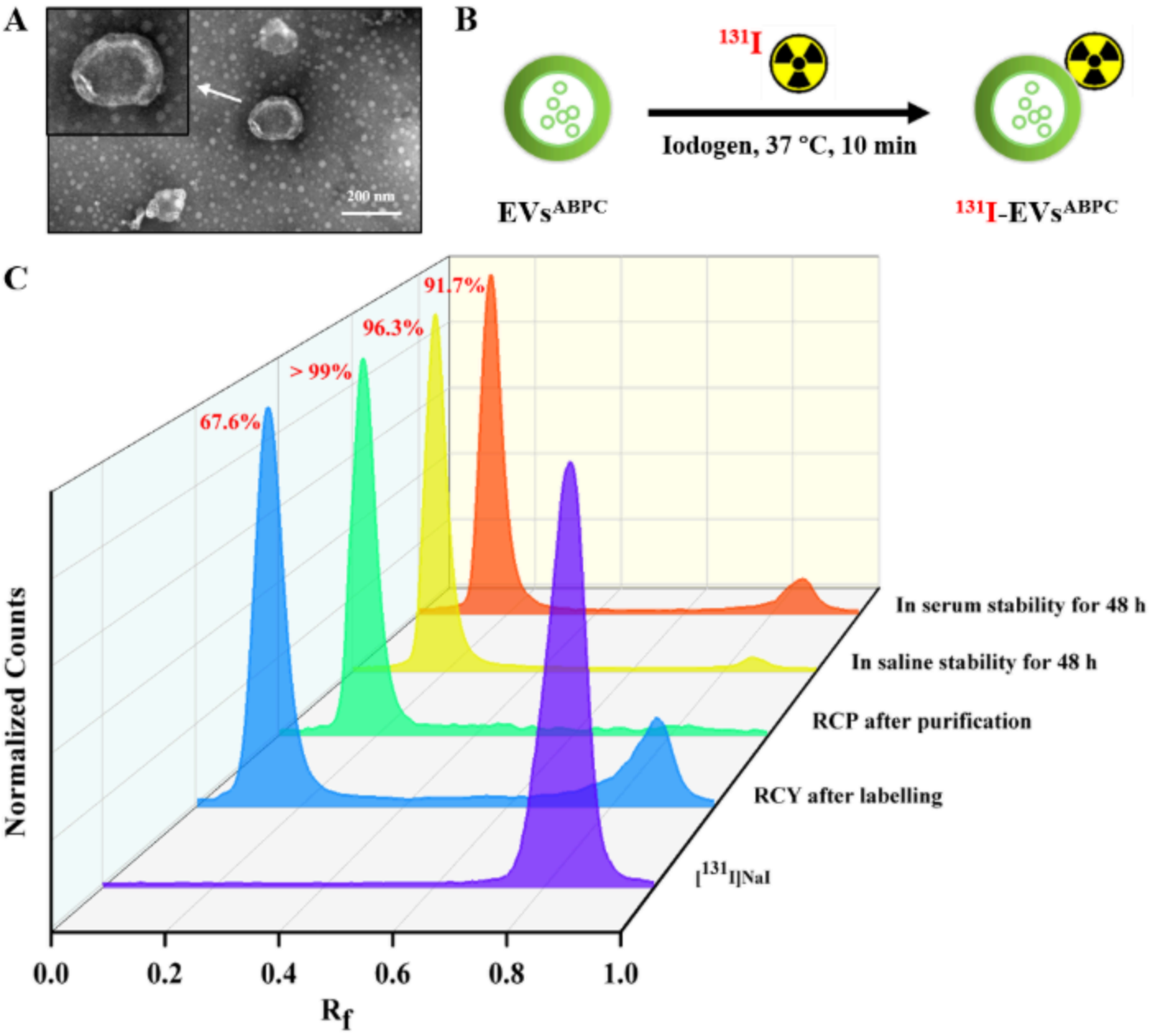


Figure 1

Preparation of ^{131}I-EVs^{ABPC}. (A) TEM characterization of EVs^{ABPC}; (B) Schematic diagram of the radiolabeling process for ^{131}I-EVs^{ABPC}; (C) *In vitro* stability evaluation of ^{131}I-EVs^{ABPC}.

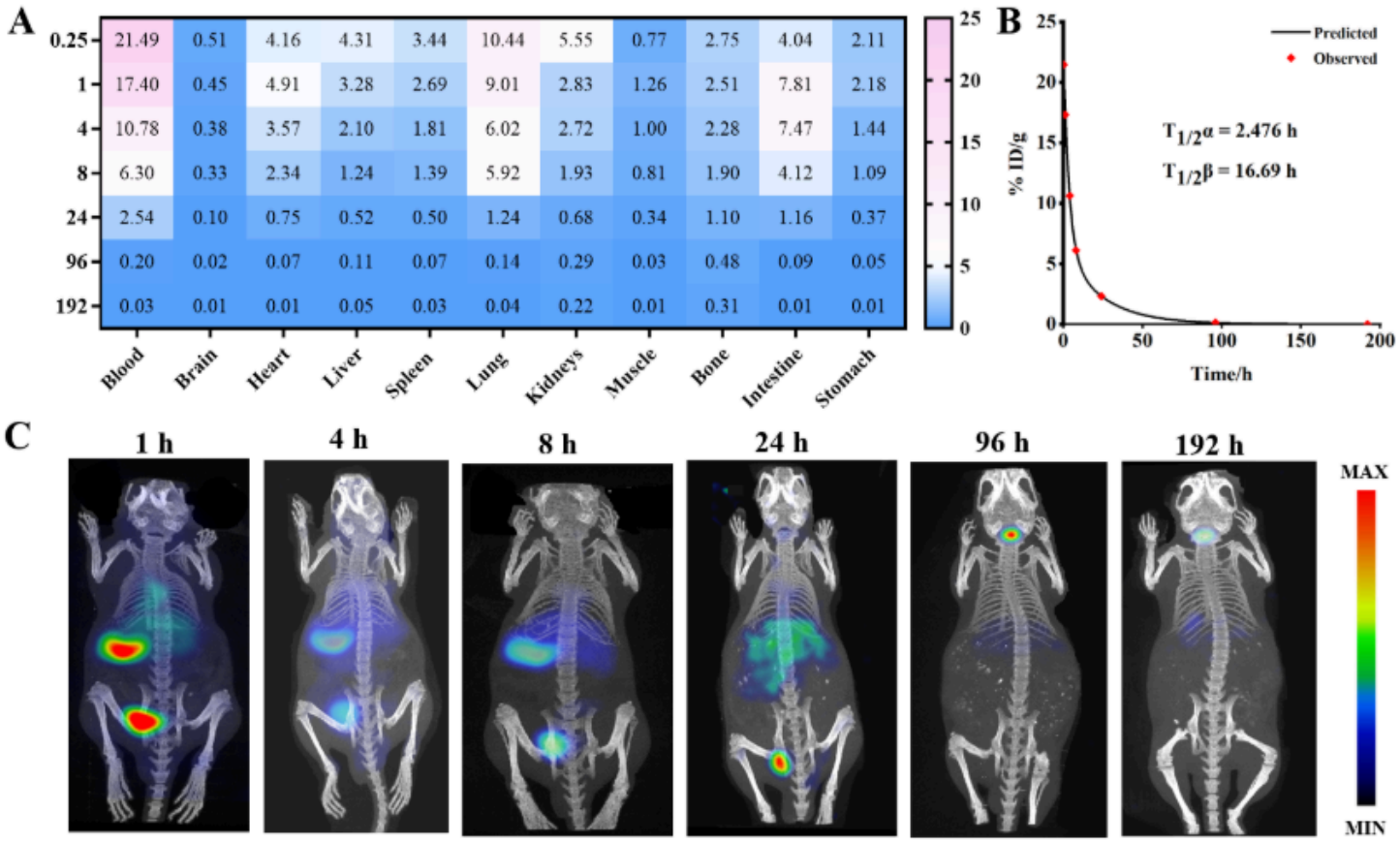


Figure 2

Biodistribution (A), time-blood concentration profile (B), and micro-SPECT/CT imaging (C) of ^{131}I-EVs^{ABPC} in mice.

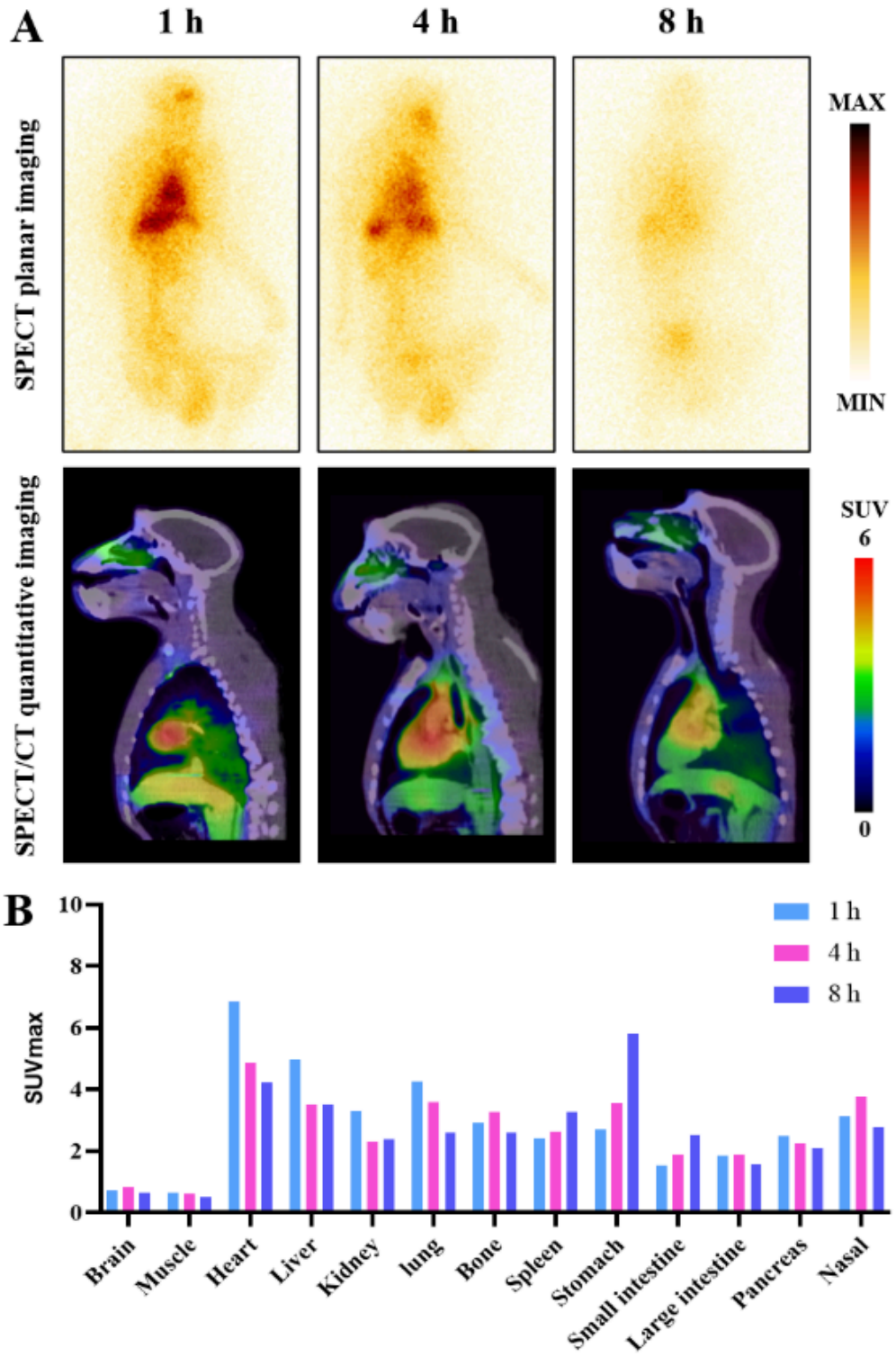


Figure 3

In vivo SPECT imaging of ^{131}I-EVs^{ABPC} in healthy macaques. (A) Planar SPECT and quantitative SPECT/CT images; (B) Organ SUV values from SPECT/CT quantification.

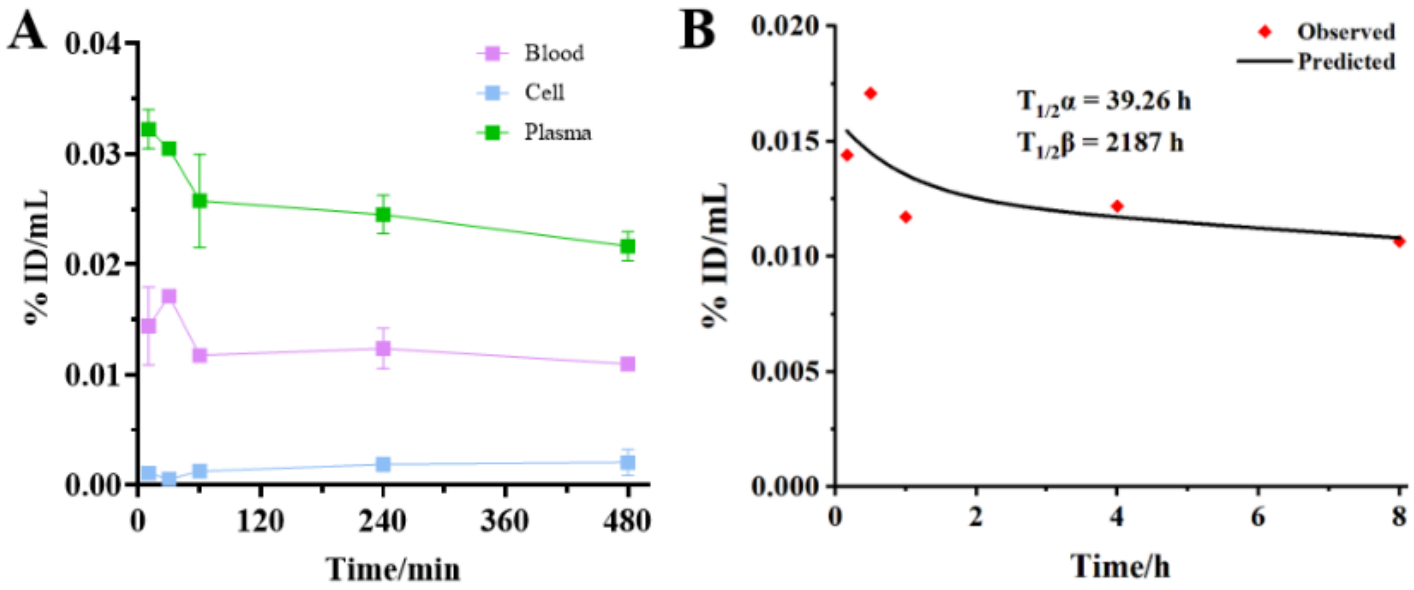


Figure 4

Blood anasysis of ^{131}I-EVs^{ABPC} in healthy macaque. radioanalysis of blood samples (A), and the time-blood concentration profile (B).

Supplementary Files

This is a list of supplementary files associated with this preprint. Click to download.

- Supplementaryinformation.docx